Steel and Composite Structures, *Vol. 38, No. 4 (2021) 415-430*
DOI: https://doi.org/10.12989/scs.2021.38.4.415

Effective width of steel-concrete composite beams under negative moments in service stages

Li Zhu[1a], Qi Ma[2b], Wu-Tong Yan[*1,3], Bing Han[1c] and Wei Liu[1d]

[1]*School of Civil Engineering, Beijing Jiaotong University, Beijing 100044, PR China*
[2]*Department of Civil and Environmental Engineering, The Hong Kong Polytechnic University, Hung Hom, Hong Kong, PR China*
[3]*China Railway Economic and Planning Research Institute, Beijing 100038, PR China*

(*Received August 22, 2019, Revised January 15, 2021, Accepted January 26, 2021*)

Abstract. The effective flange width was usually introduced into elementary beam theory to consider the shear lag effect in steel-concrete composite beams. Previous studies have primarily focused on the effective width under positive moments and elastic loading, whereas it is still not clear for negative moment cases in the normal service stages. To account for this problem, this paper proposed simplified formulas for the effective flange width and reinforcement stress of composite beams under negative moments in service stages. First, a 10-degree-of-freedom (DOF) fiber beam element considering the shear lag effect and interfacial slip effect was proposed, and a computational procedure was developed in the OpenSees software. The accuracy and applicability of the proposed model were verified through comparisons with experimental results. Second, a method was proposed for determining the effective width of composite beams under negative moments based on reinforcement stress. Employing the proposed model, the simplified formulas were proposed via numerical fitting for cases under uniform loading and centralized loading at the mid-span. Finally, based on the proposed formulas, a simplified calculation method for the reinforcement stress in service stages was established. Comparisons were made between the proposed formulas and design code. The results showed that the design code method greatly underestimated the contribution of concrete under negative moments, leading to notable overestimations in the reinforcement stress and crack width.

Keywords: effective flange width; composite beams; negative moments; fiber beam element

1. Introduction

Steel-concrete composite beams have been widely used in structural engineering applications in recent years due to their high bearing capacity, light weight and convenient construction. With a wide concrete flange, the shear lag effect will be obviously observed, and the longitudinal displacement along the slab width will not be uniformly distributed (Ma *et al.* 2017). This shear lag effect will significantly affect the bearing capacity and stiffness of structures (Luo *et al.* 2019), which is a key problem that cannot be ignored in structural analysis.

The numerical models involved in the calculation of the shear lag effect of composite beams are mainly refined models and frame models (Vojnić-Purčar *et al.* 2019). In refined models, two-dimensional shell or three-dimensional solid elements can be used to simulate the non-uniform transverse deformation of concrete slabs. However, these models are not practical in practice due to their complex modeling process and low computational efficiency. Frame models based on one-dimensional beam elements are the preferred and more widely used option. At present, some studies have focused on frame models, for which the modeling idea is to introduce the intensity function and shape function along the transverse of the shear lag effect on the basis of Euler beams. Dezi *et al.* (2003, 2006), Ranzi and Bradford (2006, 2009) and Gara *et al.* (2009, 2011) carried out representative research in this field. On the basis of one-dimensional Euler beam theory, they proposed one-dimensional models of composite beams considering shear lag and interfacial slip by adding the longitudinal displacements of steel and concrete and the shear lag strength function of concrete slabs. The proposed one-dimensional models were suitable for the design analysis of the composite decks of long-span bridges with complex geometry, such as cable stayed bridges. Lezgy-Nazargah and Kafi (2015) proposed a finite element model for the analysis of steel-concrete composite beams based on a refined high-order theory. Lezgy-Nazargah *et al.* (2019) proposed a sinus shear deformation model for static analysis of steel-concrete concrete beams and twin-girder decks including shear lag and interfacial slip effects. Furthermore, the shrinkage and creep constitutive function of concrete was also introduced into the one-dimensional model to consider the time-dependent behavior of composite beams.

*Corresponding author, Ph.D.
E-mail: yanwutong@bjtu.edu.cn
[a]Associate Professor
E-mail: zhuli@bjtu.edu.cn
[b] Ph.D. Student
E-mail: 20032544r@connect.polyu.hk
[c]Professor
E-mail: bhan@bjtu.edu.cn
[d]Master Student
E-mail: 19121073@bjtu.edu.cn

Copyright © 2021 Techno-Press, Ltd.
http://www.techno-press.org/?journal=scs&subpage=8
ISSN: 1229-9367 (Print), 1598-6233 (Online)

Zhu and Su (2017) established analytical solutions of composite beams considering shear lag and interfacial slip. Moreover, a new one-dimensional model calculation method for time-dependent behavior was proposed based on the step-by-step calculation method. However, these models can only be applied to the elastic analysis of composite beams and cannot be used to analyze plastic behavior, such as concrete cracking, concrete crushing and steel girder yielding. Lin and Zhao (2012) analyzed the elastoplastic behavior by reducing the elastic modulus on the basis of the one-dimensional beam theory. However, this method was only an approximate treatment, which cannot be used to analyze the evolution of the shear lag effect of composite beams over the whole elastoplastic loading process. Yoon *et al.* (2017) proposed an efficient warping model for elastoplastic torsional analysis of steel-concrete composite beams. However, the shear lag effect of composite beams was not included in the warping model. Therefore, a one-dimensional beam element model considering shear lag and interfacial slip for composite beams under elastic-plastic loading is needed to be developed.

Effective flange width has been introduced into design codes to simplify the consideration of the shear lag effect. It is generally believed that due to the shear lag effect, the cross-sectional stress is not uniform along the transverse direction. Based on the peak stress along the transverse direction, the actual plate width should be reduced in the calculation of the Euler beam, and this reduced flange width is called the effective width. Amadio and Fragiacomo (2002) carried out experiments of composite beams under positive and negative moments to study the effective width of concrete flanges, which contributed to the provisions of the EC4 code (2004). Chiewanichakorn *et al.* (2004) and Chen *et al.* (2007) proposed a simplified formula for calculating the effective width by considering the effect of the concrete slab thickness, and they determined that the effective width was close to the actual width. Zhu *et al.* (2015) systematically studied the effective width of concrete slabs and steel bottom slabs of composite beams. In their study, effective width formulas were proposed for composite beams under vertical and axial loads, and a simplified method was also developed to consider the shear lag effect. Nie *et al.* (2008) studied the effective width of composite beams under ultimate positive bending through a combination of experiments and numerical analysis and concluded that the effective width was close to the actual width under ultimate states. Based on these studies, it can be concluded that the effective width of composite beams is generally smaller than the actual width in the elastic stage and increases with plastic development until the limit state. At the ultimate capacity state, the effective width is equal to the actual width. However, current research on the effective width evolution during the whole elastoplastic process is still insufficient. Moreover, concrete cracking under a negative moment, which should receive attention, occurs even in normal service. After cracking, concrete quickly loses its strength, and the reinforcement stress is not evenly distributed. Some design codes neglect the role of concrete slabs after cracking, and only steel beams and reinforcements in the effective width range are considered. This assumption is applicable only for the ultimate capacity state under a negative moment. For other states, this assumption will overestimate the reinforcement stress and crack width of the concrete slab, seriously affecting the design scheme. Therefore, it is of great significance to study the effective width of composite beams under elastic-plastic loading states, especially for cases under negative moments.

In this paper, a 10-degree-of-freedom (DOF) fiber beam element considering the shear lag and interfacial slip of a composite beam over the whole elastoplastic loading process is proposed and implemented on the OpenSees software framework. Furthermore, the accuracy and applicability of the proposed model are verified by comparing with the experiments of composite beams under positive and negative bending moments. Then, the model is employed to analyze the features and development of the effective width under a negative moment in the normal service stage. The key influencing factors of effective width are refined and discussed through a parameter sensitivity analysis. Finally, a simplified calculation method is proposed for the effective flange width under a negative moment in the normal service stage.

2. Fiber beam element considering interfacial slip and shear lag effects

The fiber beam element proposed in this paper is applicable to composite beams with open cross-sections, as shown in Fig. 1. Interfacial slip, shear lag effects and material nonlinear behavior are all considered in the model. The coordinate system and the symbol annotation are shown in Fig. 1. Fig. 2 shows the fiber divisions of the composite cross-section.

2.1 Kinematics

The proposed beam element model is a two-dimensional model without considering transverse bending and torsion of composite beams

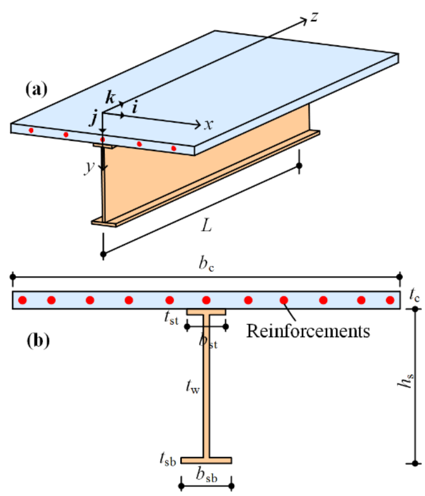

Fig. 1 Cross-section and coordinate system for the composite beam: (a) three-dimensional view and (b) cross-sectional view

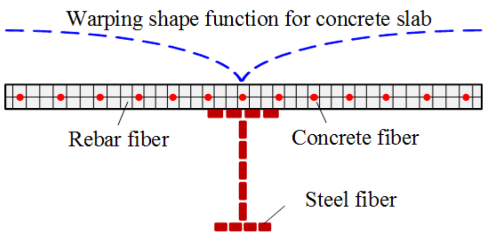

Fig. 2 Fiber divisions for the composite cross-section

This beam element model uses the kinematics of composite I-shape beams proposed by Dezi *et al.* (2003, 2006), Ranzi and Bradford (2006, 2009) and Gara *et al.* (2009, 2011). The steel girder and concrete slab cannot be separated vertically, but longitudinal slip occurs at the slab-girder interface of the composite beam. The concrete slab and steel girder have the same curvature. The steel girder is modeled with the Euler-Bernoulli beam theory consistent with the plane section assumption. The shear lag warping function is introduced into the concrete model to consider the non-uniform distribution of longitudinal displacement in the transverse direction. Referring to the coordinate system shown in Fig. 1, the displacement field function of the composite beams can be expressed as

$$\begin{cases} u_c(x,y,z) = u_{c0}(z) - v_0'(z)y + f(z)\psi(x) \\ u_s(x,y,z) = u_{s0}(z) - v_0'(z)y \\ v(x,y,z) = v_0(z) \end{cases} \tag{1}$$

where $v_0(z)$ and $v_0'(z)$ are the vertical displacement and rotation of the composite cross-section, $u_c(z)$ denotes the axial displacement of the concrete slab at any position, u_{c0} denotes the whole longitudinal displacement of the concrete slab at its centroid position, $u_s(z)$ denotes the axial displacement of the steel girder at any position, $u_{s0}(z)$ denotes the whole longitudinal displacement of the steel girder at its centroid position, and $f(z)$and $\psi(x)$ represent the warping intensity and shape function of concrete slab, respectively.

The warping function $\psi(x)$ describing the shear lag effect should satisfy ψ=0 at the intersection of the concrete slab and the steel beam web and $\psi_{,x}$=0 on the edge of concrete slab. Thus, $\psi(x)$ in this paper is adopted as follows. For I-steel composite beams

$$\psi(x) = -\left[1 - \left(1 - \frac{2|x|}{b_c}\right)^2\right] \tag{2}$$

According to the geometric equation, the strain tensor of composite beams can be expressed as,

$$\begin{cases} \varepsilon_{cz}(x,y,z) = u_{c0}' - yv_0'' + f'\psi \\ \varepsilon_{sz}(x,y,z) = u_{s0}' - yv_0'' \\ \gamma_{cxz}(x,y,z) = f\psi_{,x} \end{cases} \tag{3}$$

Furthermore, the interfacial slip between the steel beam and the concrete slab is

$$\Gamma(z) = u_s(z) - u_c(z) \tag{4}$$

2.2 Constitutive relationship

The constitutive equations of four commonly adopted materials are considered in this study: elastic material, concrete material, steel material, and reinforcement material.

The uniaxial constitutive relation of materials is a physical nonlinear description of fiber level, which is the basis of the section stiffness matrix and the element stiffness matrix. According to the requirements of this study, the following constitutive functions are adopted for modeling the concrete, steel girder, reinforcement and interfacial slip.

(1) Concrete

Fig. 3(a) shows the uniaxial stress-strain curve of the concrete. The compressive stress-strain relationship is assumed in the parabolic-ascending linear-descending form proposed by Hognestad *et al.* (1955), as stated in Eq. (5). In Eq. (5), ε_{c0} is the peak compressive strain and the peak compressive stress σ_{c0} is equal to the cylinder concrete compressive strength f_c. The concrete softening stiffness is determined by the data point (ε_{cu}, 0). To mitigate mesh sensitivity problems, ε_{cu} is set as a mesh-adjusted strain, which is specified by the characteristic length of the respective finite element (FE) integration point and volume-specific localized crushing energy (Wendner *et al.* 2015). The initial tangent modulus of concrete E_c=2$\sigma_{c0}/\varepsilon_{c0}$.

The tensile stress-strain relationship is shown in Eq. (6), and the curve is shown in Fig. 3(a). The peak tensile stress $\sigma_{t0}=f_t$, in which f_t is the concrete tensile strength and the peak tensile strain $\varepsilon_{t0}=f_t/E_c$. The smeared crack model is employed to simulate the tension softening behavior of concrete after cracking. According to the crack band theory, the ultimate tensile strain ε_{tu} can be determined with the concrete fracture energy G_f, which is provided in CEB-FIP (2010). The tension softening stiffness E_{ts} can be expressed as $E_{ts}=\sigma_{t0}/(\varepsilon_{tu}-\varepsilon_{t0})$.

$$\sigma = \begin{cases} \sigma_{c0}\left[2\left(\dfrac{\varepsilon}{\varepsilon_{c0}}\right) - \left(\dfrac{\varepsilon}{\varepsilon_{c0}}\right)^2\right] & \varepsilon_{c0} \le \varepsilon \le 0 \\ \sigma_{c0}\left[1 - \left(\dfrac{\varepsilon - \varepsilon_{c0}}{\varepsilon_{cu} - \varepsilon_{c0}}\right)\right] & \varepsilon \le \varepsilon_{c0} \end{cases} \tag{5}$$

$$\sigma = \begin{cases} E_c \cdot \varepsilon, & 0 \le \varepsilon \le \varepsilon_{t0} \\ \sigma_{t0} - E_{ts}(\varepsilon - \varepsilon_{t0}), & \varepsilon_{t0} \le \varepsilon \le \varepsilon_{tu} \end{cases} \tag{6}$$

The shear constitutive model in concrete is assumed to be a linear elastic constitutive relation because a sufficient number of stirrups are usually arranged in practice to prevent shear failure. The shear modulus G_c was calculated as $G_c=E_c/2/(1+\nu_c)$, in which ν_c is the Poisson's ratio of concrete, which is generally 0.2.

(2) Steel girder and reinforcement

The trilinear model with a yield plateau is adopted for

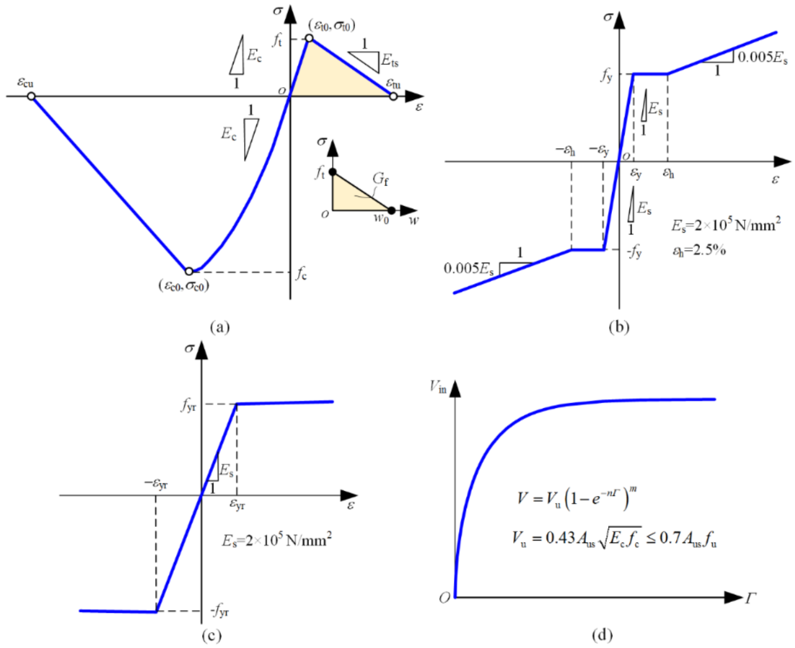

Fig. 3 Uniaxial constitutive relationships for the materials: (a) concrete, (b) steel, (c) reinforcement and (d) beam-slab interface

the steel material, as shown in Fig. 3(b), in which E_s is the initial tangent modulus, the hardening modulus is $0.005E_s$, and ε_h denotes the hardening strain, which is generally 0.025. The elastic-perfectly plastic model is adopted for the reinforcement material, as shown in Fig. 3(c). The reinforcement fiber shear stiffness does not contribute to the section stiffness; thus, the shear modulus of the reinforcement material is 0.

(3) Beam-slab interfacial slip

The slip constitutive relationships for stud connections proposed by Ollgaard *et al.* (1971) are adopted to model the interfacial slip between the steel girder and concrete slab

$$V_{in} = V_u\left(1-e^{-n\Gamma}\right)^m \tag{7}$$

where V_{in} is the shear force on the interface; n and m are constant values, which are generally m=0.558 and n=1 mm^{-1}; and V_u is the ultimate capacity of a single stud, which can be determined with Eq. (8); Γ=u_{s0}-u_{c0} and is the interfacial slip between the steel girder and the concrete slab.

$$V_u = 0.43A_{us}\sqrt{E_c f_c} \le 0.7A_{us}f_u \tag{8}$$

where f_u denotes the ultimate tensile strength of the shear stud and A_{us} is the cross-sectional area of the shear stud.

2.3 Balance conditions

According to the virtual work principle, an equilibrium equation can be established as

$$\int_V \boldsymbol{S}\cdot\nabla\left(\hat{\boldsymbol{d}}\right) = \int_V \boldsymbol{b}\cdot\hat{\boldsymbol{d}} + \int_{\partial V}\boldsymbol{s}\cdot\hat{\boldsymbol{d}} \qquad \forall\hat{\boldsymbol{d}}\neq 0 \tag{9}$$

where $\boldsymbol{S}$ is the Cauchy symmetric stress tensor, ∇ is the gradient operator, $\hat{\boldsymbol{d}}$ is the variation in the displacement field, $\boldsymbol{b}$ is the body force, $\boldsymbol{s}$ is the surface force applied to composite beams, V denotes the body integration domain, and ∂V denotes the surface integration domain.

For the I-steel composite beams in this study, the generalized displacement vector can be defined as

$$\boldsymbol{d} = \left[u_{c0} \quad u_{s0} \quad v_0 \quad f\right]^{\mathrm{T}} \tag{10}$$

The generalized displacement increment can be expressed as

$$\Delta\boldsymbol{d} = \left[\Delta u_{c0} \quad \Delta u_{s0} \quad \Delta v_0 \quad \Delta f\right]^{\mathrm{T}} \tag{11}$$

For an incremental displacement, the virtual work principle is considered, which is expressed as

$$\begin{aligned}&\int_0^L\left[\left[\boldsymbol{K}_c(z)+\boldsymbol{K}_r(z)+\boldsymbol{K}_s(z)+\boldsymbol{K}_p(z)\right]\mathscr{D}\left(\Delta\boldsymbol{d}(z)\right)\right]\cdot\mathscr{D}\left(\Delta\hat{\boldsymbol{d}}\right)\mathrm{d}z\\&=\int_0^L\boldsymbol{p}(z)\cdot\mathscr{K}\left(\Delta\hat{\boldsymbol{d}}\right)\mathrm{d}z \qquad \forall\left(\Delta\hat{\boldsymbol{d}}\right)\neq 0\end{aligned} \tag{12}$$

where

$$\left(\mathscr{D}(\Delta\boldsymbol{d})\right) = \left[\Delta u_{c0}' \quad \Delta u_{s0}' \quad -\Delta v_0'' \quad \Delta f' \quad \Delta f \quad \Delta u_{s0}-\Delta u_{c0}\right]^{\mathrm{T}} \tag{13}$$

$$\left(\mathscr{K}(\Delta\boldsymbol{d})\right) = \left[\Delta u_{c0} \quad \Delta u_{s0} \quad \Delta v_0 \quad -\Delta v_0' \quad \Delta f\right]^{\mathrm{T}} \tag{14}$$

By defining the different fibers, the proposed model can be applied to structures with different types of cross-sections. The fiber stiffness can be updated with respect to changes in the stress states during the elastoplastic iterative process. This approach is different from other approaches found in existing research, which are insufficient for the application of different types of cross-sections and plastic loading stages. Based on the idea of fiber discretization, the integral calculation of the section stiffness matrix and resistance vector is carried out by the algebraic summation of discrete fibers, as shown in Eqs. (15) and (16).

$$\boldsymbol{K}_{\mathbf{c}}(z)=\begin{bmatrix} \sum_{k=1}^{N_c} E_{ck}A_{ck} & 0 & -\sum_{k=1}^{N_c} E_{ck}A_{ck}y_{ck} & \sum_{k=1}^{N_c} E_{ck}A_{ck}\psi_{ck} & 0 & 0 \\ 0 & 0 & 0 & 0 & 0 & 0 \\ -\sum_{k=1}^{N_c} E_{ck}A_{ck}y_{ck} & 0 & \sum_{k=1}^{N_c} E_{ck}A_{ck}y_{ck}^2 & -\sum_{k=1}^{N_c} E_{ck}A_{ck}y_{ck}\psi_{ck} & 0 & 0 \\ \sum_{k=1}^{N_c} E_{ck}A_{ck}\psi_{ck} & 0 & -\sum_{k=1}^{N_c} E_{ck}A_{ck}y_{ck}\psi_{ck} & \sum_{k=1}^{N_c} E_{ck}A_{ck}\psi_{ck}^2 & 0 & 0 \\ 0 & 0 & 0 & 0 & \sum_{k=1}^{N_c} G_{ck}A_{ck}\psi_{,xck}^2 & 0 \\ 0 & 0 & 0 & 0 & 0 & 0 \end{bmatrix} \tag{15a}$$

$$\boldsymbol{K}_{\mathbf{r}}(z)=\begin{bmatrix} \sum_{k=1}^{N_r} E_{rk}A_{rk} & 0 & -\sum_{k=1}^{N_r} E_{rk}A_{rk}y_{rk} & \sum_{k=1}^{N_r} E_{rk}A_{rk}\psi_{rk} & 0 & 0 \\ 0 & 0 & 0 & 0 & 0 & 0 \\ -\sum_{k=1}^{N_r} E_{rk}A_{rk}y_{rk} & 0 & \sum_{k=1}^{N_r} E_{rk}A_{rk}y_{rk}^2 & -\sum_{k=1}^{N_r} E_{rk}A_{rk}y_{rk}\psi_{rk} & 0 & 0 \\ \sum_{k=1}^{N_r} E_{rk}A_{rk}\psi_{rk} & 0 & -\sum_{k=1}^{N_r} E_{rk}A_{rk}y_{rk}\psi_{rk} & \sum_{k=1}^{N_r} E_{rk}A_{rk}\psi_{rk}^2 & 0 & 0 \\ 0 & 0 & 0 & 0 & 0 & 0 \\ 0 & 0 & 0 & 0 & 0 & 0 \end{bmatrix} \tag{15b}$$

$$\boldsymbol{K}_{\mathbf{s}}(z)=\begin{bmatrix} 0 & 0 & 0 & 0 & 0 & 0 \\ 0 & \sum_{k=1}^{N_s} E_{sk}A_{sk} & -\sum_{k=1}^{N_s} E_{sk}A_{sk}y_{sk} & 0 & 0 & 0 \\ 0 & -\sum_{k=1}^{N_s} E_{sk}A_{sk}y_{sk} & \sum_{k=1}^{N_s} E_{sk}A_{sk}y_{sk}^2 & 0 & 0 & 0 \\ 0 & 0 & 0 & 0 & 0 & 0 \\ 0 & 0 & 0 & 0 & 0 & 0 \\ 0 & 0 & 0 & 0 & 0 & 0 \end{bmatrix} \tag{15c}$$

$$\boldsymbol{K}_{\boldsymbol{\rho}}(z)=\begin{bmatrix} 0 & 0 & 0 & 0 & 0 & 0 \\ 0 & 0 & 0 & 0 & 0 & 0 \\ 0 & 0 & 0 & 0 & 0 & 0 \\ 0 & 0 & 0 & 0 & 0 & 0 \\ 0 & 0 & 0 & 0 & 0 & 0 \\ 0 & 0 & 0 & 0 & 0 & \rho \end{bmatrix} \tag{15d}$$

$$\boldsymbol{K}(z)=\boldsymbol{K}_{\mathbf{c}}(z)+\boldsymbol{K}_{\mathbf{r}}(z)+\boldsymbol{K}_{\mathbf{s}}(z)+\boldsymbol{K}_{\boldsymbol{\rho}}(z) \tag{15e}$$

where ρ denotes the tangent stiffness of the shear-slip relationship in Eq. (7), N_c denotes the number of concrete fibers, N_r denotes the number of steel fibers, and N_s denotes the number of reinforcement fibers.

The resistance vector can be expressed as

$$\boldsymbol{R}_{\mathbf{c}}(z)=\begin{bmatrix} \sum_{k=1}^{N_c} \sigma_{ck}A_{ck} & 0 & -\sum_{k=1}^{N_c} \sigma_{ck}A_{ck}y_{ck} & \sum_{k=1}^{N_c} \sigma_{ck}A_{ck}\psi_{ck} & \sum_{k=1}^{N_c} \tau_{ck}A_{ck}\psi_{,xck} & 0 \end{bmatrix}^{\mathrm{T}} \tag{16a}$$

$$\boldsymbol{R}_{\mathbf{r}}(z)=\begin{bmatrix} \sum_{k=1}^{N_r} \sigma_{rk}A_{rk} & 0 & -\sum_{k=1}^{N_r} \sigma_{rk}A_{rk}y_{rk} & \sum_{k=1}^{N_r} \sigma_{rk}A_{rk}\psi_{rk} & 0 & 0 \end{bmatrix}^{\mathrm{T}} \tag{16b}$$

$$\boldsymbol{R}_{\mathbf{s}}(z)=\begin{bmatrix} 0 & \sum_{k=1}^{N_s} \sigma_{sk}A_{sk} & -\sum_{k=1}^{N_s} \sigma_{sk}A_{sk}y_{sk} & 0 & 0 & 0 \end{bmatrix}^{\mathrm{T}} \tag{16c}$$

$$\boldsymbol{R}_{\mathbf{p}}(z)=\begin{bmatrix}0 & 0 & 0 & 0 & 0 & V_{\text{in}}\end{bmatrix}^{\mathrm{T}} \tag{16d}$$

$$\boldsymbol{R}(z)=\boldsymbol{R}_{\mathbf{c}}(z)+\boldsymbol{R}_{\mathbf{r}}(z)+\boldsymbol{R}_{\mathbf{s}}(z)+\boldsymbol{R}_{\mathbf{p}}(z) \tag{16e}$$

The external load $\boldsymbol{p}$ is

$$\boldsymbol{p}(z)=\begin{bmatrix}q_{\text{cz}} & q_{\text{sz}} & q_y & m_x & \omega_{\text{c}}\end{bmatrix} \tag{17a}$$

$$q_{\text{cz}}(z)=\int_{\Omega_{\text{c}}} b_z \mathrm{d}a+\int_{\partial\Omega_{\text{c}}} s_z \mathrm{d}l \tag{17b}$$

$$q_{\text{sz}}(z)=\int_{\Omega_{\text{s}}} b_z \mathrm{d}a+\int_{\partial\Omega_{\text{s}}} s_z \mathrm{d}l \tag{17c}$$

$$q_y(z)=\int_{\Omega} b_y \mathrm{d}a+\int_{\partial\Omega} s_y \mathrm{d}l \tag{17d}$$

$$m_x(z)=\int_{\Omega} b_z y \mathrm{d}a+\int_{\partial\Omega} s_z y \mathrm{d}l \tag{17e}$$

$$\omega_{\text{c}}(z)=\int_{\Omega_{\text{c}}} b_z \psi \mathrm{d}a+\int_{\partial\Omega_{\text{c}}} s_z \psi \mathrm{d}l \tag{17f}$$

where Ω, Ω_{c} and Ω_{s} denote the volume integral domains of the whole structure, concrete and steel girder, respectively, and $\partial\Omega$, $\partial\Omega_{\text{c}}$ and $\partial\Omega_{\text{s}}$ are the corresponding surface integral domains.

2.4 Numerical procedures

The FE method is adopted to solve the equations. A 10-DOF beam element is proposed in this paper, and the nodal displacement $\boldsymbol{\delta}_{\mathbf{e}}$ and the resistance vector $\boldsymbol{R}_{\mathbf{e}}$ can be expressed as

$$\boldsymbol{\delta}_{\text{e}}=\begin{bmatrix}u_{ci} & u_{si} & v_i & \theta_i & f_i & u_{cj} & u_{sj} & v_j & \theta_j & f_j\end{bmatrix}^{\mathrm{T}}$$

$$\boldsymbol{R}_{\text{e}}=\begin{bmatrix}N_{ci} & N_{si} & V_i & M_i & W_i & N_{cj} & N_{sj} & V_j & M_j & W_j\end{bmatrix}^{\mathrm{T}}$$

The deformation field inside the element can be interpolated with the Hermite polynomial interpolation method. For the vertical deflection v and the rotation θ, the second-order Hermite displacement difference is used. For u_{c}, u_{s} and f, the first-order linear interpolation is used. The shape function matrix $\boldsymbol{N}_{\mathbf{e}}$ can be expressed as

$$\boldsymbol{d}=\boldsymbol{N}_{\mathbf{e}}^{\mathrm{T}}\boldsymbol{\delta}_{\mathbf{e}} \tag{18}$$

where

$$\boldsymbol{N}_{\text{e}}(\xi)=\begin{bmatrix}1-\lambda & 0 & 0 & 0\\ 0 & 1-\lambda & 0 & 0\\ 0 & 0 & 1-3\lambda^2+2\lambda^3 & 0\\ 0 & 0 & L_{\text{e}}\left(\lambda-2\lambda^2+\lambda^3\right) & 0\\ 0 & 0 & 0 & 1-\lambda\\ \lambda & 0 & 0 & 0\\ 0 & \lambda & 0 & 0\\ 0 & 0 & 3\lambda^2-2\lambda^3 & 0\\ 0 & 0 & L_{\text{e}}\left(-\lambda^2+\lambda^3\right) & 0\\ 0 & 0 & 0 & \lambda\end{bmatrix}^{\mathrm{T}}$$

Note that $\lambda=\xi/L_{\text{e}}$, in which ξ is the local coordinate of the beam element and L_{e} is the length of the element.

Substituting Eq. (18) into Eq. (12) yields

$$\boldsymbol{K}_{\mathbf{e}}\,\Delta\boldsymbol{\delta}_{\mathbf{e}}=\boldsymbol{F}_{\mathbf{p}} \tag{19}$$

where

$$\boldsymbol{K}_{\mathbf{e}}=\int_0^{L_{\text{e}}}\left(\mathscr{D}\boldsymbol{N}_{\mathbf{e}}\right)^{\mathrm{T}}\left(\boldsymbol{K}_{\mathbf{c}}+\boldsymbol{K}_{\mathbf{r}}+\boldsymbol{K}_{\mathbf{s}}+\boldsymbol{K}_{\boldsymbol{\rho}}\right)\left(\mathscr{D}\boldsymbol{N}_{\mathbf{e}}\right)\mathrm{d}\xi \tag{20a}$$

$$\boldsymbol{F}_{\mathbf{p}}=\int_0^{L_{\text{e}}}\left(\mathscr{H}\boldsymbol{N}_{\mathbf{e}}\right)^{\mathrm{T}}\boldsymbol{p}\,\mathrm{d}\xi \tag{20b}$$

$$\boldsymbol{R}_{\mathbf{e}}=\int_0^{L_{\text{e}}}\left(\mathscr{D}\boldsymbol{N}_{\mathbf{e}}\right)^{T}\left(\boldsymbol{R}_{\mathbf{c}}+\boldsymbol{R}_{\mathbf{r}}+\boldsymbol{R}_{\mathbf{s}}+\boldsymbol{R}_{\boldsymbol{\rho}}\right)\mathrm{d}\xi \tag{20c}$$

Note that $\boldsymbol{K}_{\mathbf{e}}$ denotes the element stiffness matrix, $\boldsymbol{F}_{\mathbf{p}}$ is the equivalent external load vector, and $\boldsymbol{R}_{\mathbf{e}}$ is the element resistance vector, which can all be obtained through Gauss-Lobatto numerical integration along the length direction of the beam.

2.5 Element implementation

The full Newton iterative method is adopted to solve the structural elastoplastic analysis problem. In each calculation step, the stiffness and stress of the fibers are updated according to the stress states, and the stiffness matrix and resistance vector are sequentially updated in the cross-section level, element level and structure level.

For flexibility, extensibility, and portability, we developed the proposed model on the computational framework of OpenSees software as a newly derived element class (Gandelli *et al.* 2019). The interpreter codes for the corresponding Tcl command were also developed. OpenSees is an open source elastic-plastic calculation software for structural engineering applications. OpenSees provides abundant material and element libraries and is a widely used computing platform for nonlinear structural analysis. However, the shear lag and interfacial slip effects are not considered in current version of OpenSees. The research and element development work in this paper provides this extended functionality. Notably, the proposed beam element model can be used to predict the elastoplastic behavior of composite beams which have an ultimate flexural failure mode.

Amadio *et al.* (2004) carried out experiments with 4 simply supported composite beams. The structural dimensions of specimen B-4 are shown in Fig. 6, and studs were set as connections between the steel beam and the concrete slab. A concentrated load was applied at the mid-span to test the mechanical behavior of the specimen under a positive bending moment up to collapse. Comparisons of the analytical and experimental results for the load-deflection at mid-span are shown in Fig. 7.

3. Case study and comparisons

3.1 Experiments of composite beams under positive moments

Li (2011) carried out an experiment on the composite girder segment of a cable-stayed bridge. The twin I-steel composite beam CSBCD-1 was selected as an analysis case,

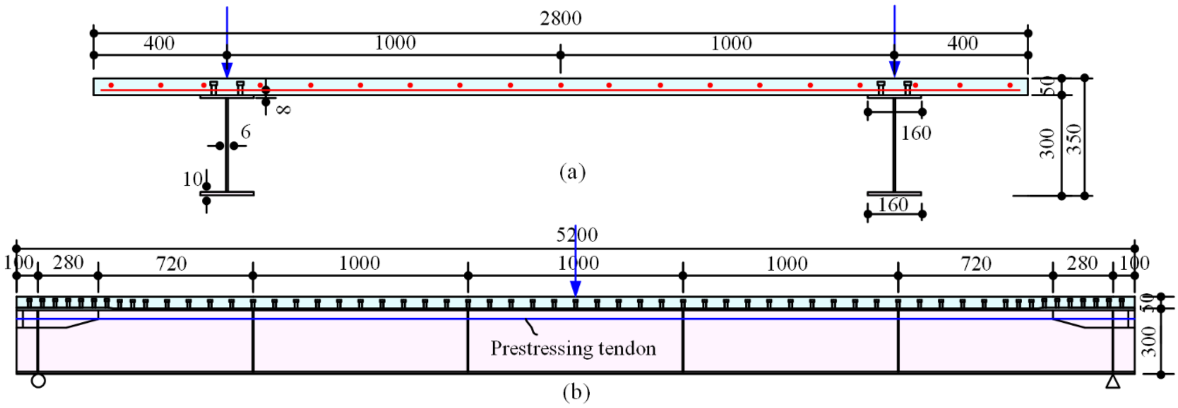

Fig. 4 Dimensions of CSBCD-1 specimens from the tests conducted by Li (2011) (unit: mm): (a) cross-section and (b) elevation

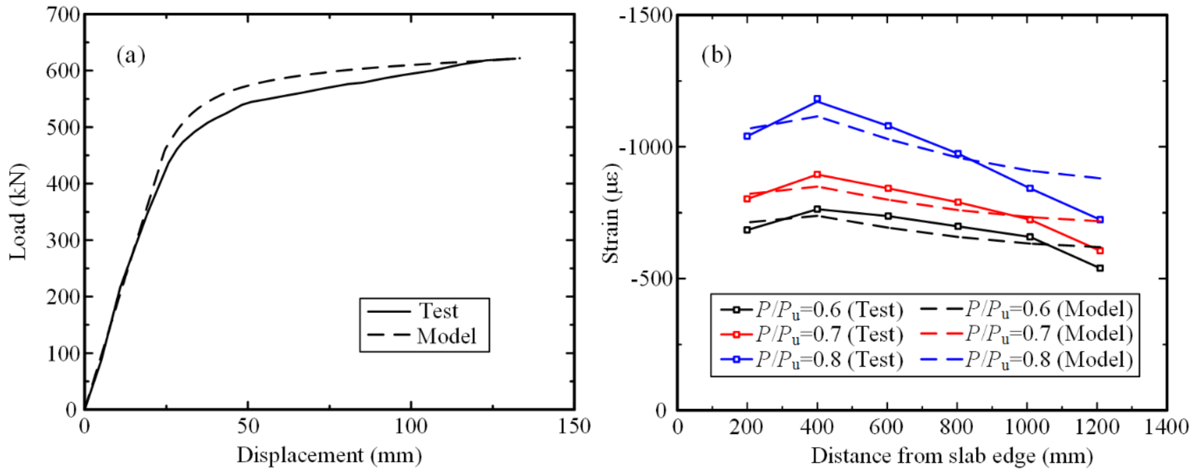

Fig. 5 Comparisons of the experimental and analytical results from the tests conducted by Li (2011): (a) load-displaceme nt response and (b) strain of concrete slab

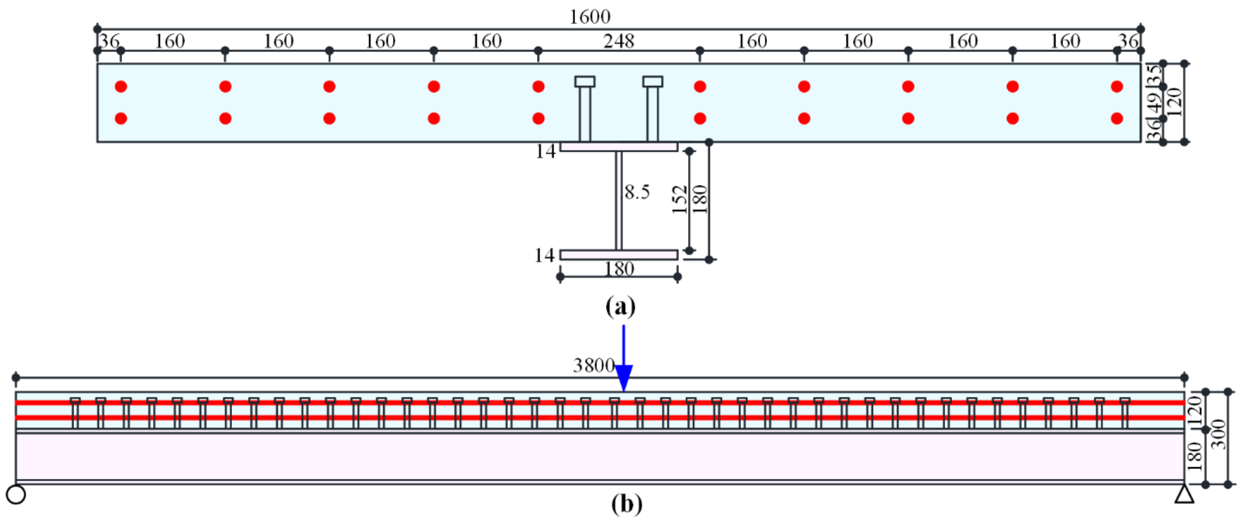

Fig. 6 Dimensions of the B-4 specimen from the tests conducted by Amadio *et al* (2004) (unit: mm): (a) cross-section and (b) elevation

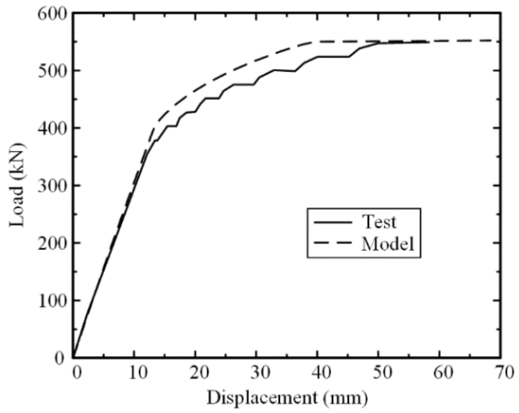

Fig. 7 Load-deflection curves of the B-4 specimen from the tests conducted by Amadio *et al* (2004)

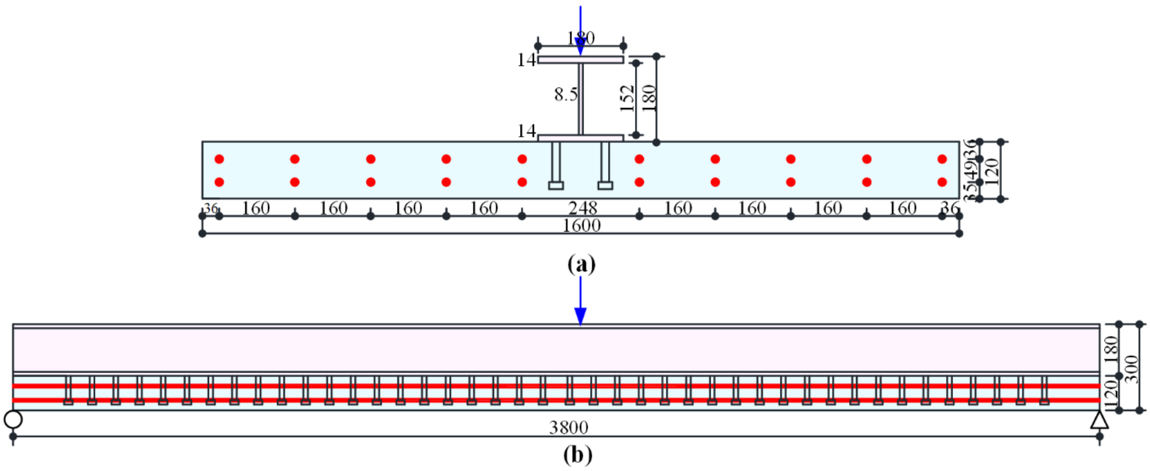

Fig. 8 Dimensions of specimen B-1 of the test conducted by Amadio *et al* (2004) (unit: mm): (a) cross-section and (b) elevation

and the dimensions of this beam are shown in Fig.4. A concentrated load was applied at the mid-span, where two-point symmetrical loading was located at the intersection of both webs and the concrete slab. The deflection and strain were measured under different loading levels up to collapse. Fig. 5 shows the load-deflection curves at the mid-span and the strain of reinforcing bars under different loading states. The comparisons show good agreement between the test results and analytical results.

3.2 Experiments of composite beams under negative moments

The experiment of a composite beam under a negative moment was also tested by Amadio *et al.* (2004), which is named B-1. The span and cross-section dimensions were the same as those of B-4, as shown in Fig. 8. The difference existed in their loading pattern. Specimen B-1 was reverse loaded, and a concentrated load was imposed on the steel beam in the mid-span to simulate a negative bending moment at the support. Fig. 9 shows comparisons of the experimental and analytical results for specimen B-1. Both the load-deflection curves and the stress distribution of the reinforcements are in good agreement between the experimental and analytical results.

Lin and Yoda (2013) performed experiments of two simply supported composite beams, in which specimen CBS was loaded under a negative moment. The structural dimensions of specimen CBS are shown in Fig. 10, and the loading pattern was the same as that of specimen B-1 in reference (Amadio *et al.* 2004). Comparisons of the results from the tests and those from the proposed model are shown in Fig. 11.

The accuracy and applicability of the proposed model were verified through comparisons with experimental results of composite beams under positive and negative moment loads.

4. Effective width under negative moment loading

In the normal service stage, under positive moment loading states, the concrete slab and steel girder are in the elastic loading range, and the effective width in this case

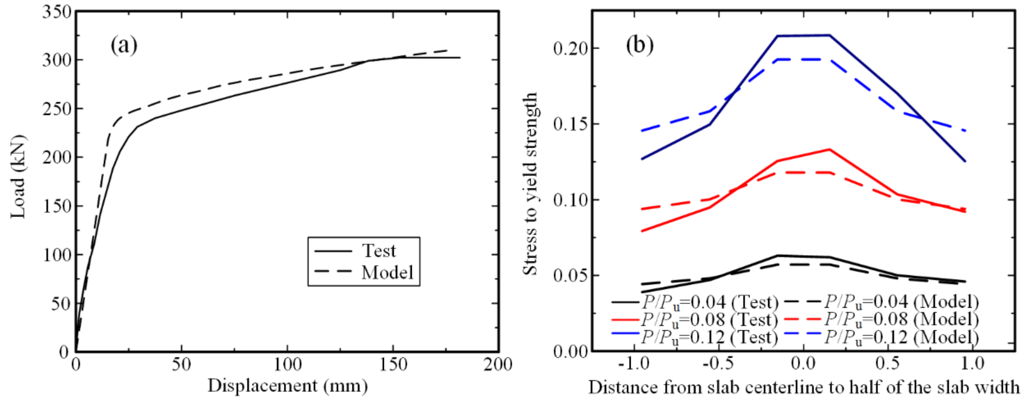

Fig. 9 Comparisons of the experimental and analytical results for specimen B-1 from the tests conducted by Amadio *et al.* (2004): (a) load-deflection curves at mid-span and (b) stress to yield strength of reinforcing bars

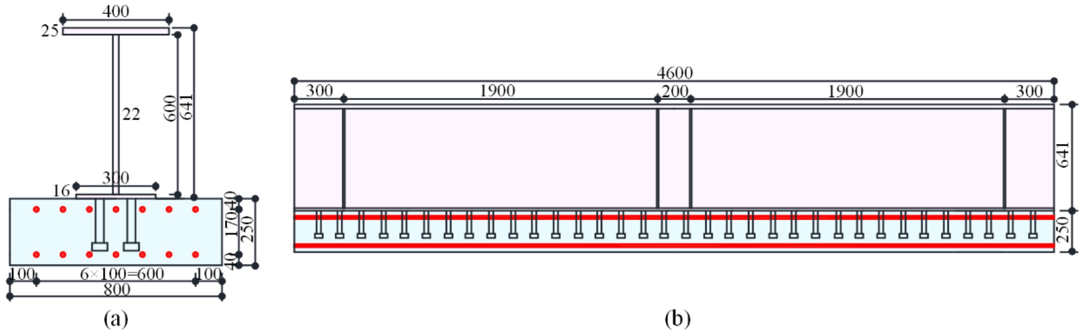

Fig. 10 Dimensions of specimen CBS from the tests by Lin and Yoda (2013) (unit: mm) : (a) cross-section and (b) elevation

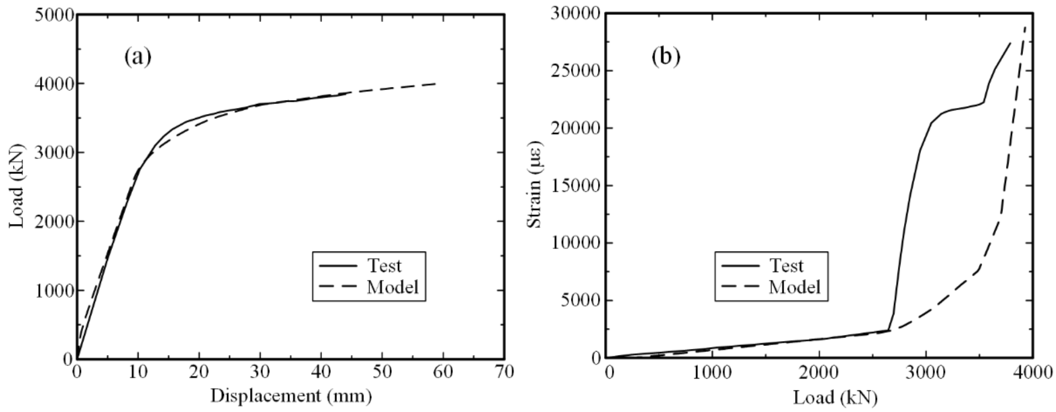

Fig. 11 Comparisons of the experimental and analytical results for specimen CBS from the tests by Lin and Yoda (2013): (a) load-displacement response and (b) strain of reinforcing bars

has been widely studied. When under negative moment loading states, even in the normal service stage, the nonlinear behavior of concrete cracking will occur, and further research is needed; this phenomenon is also a focus of this paper. Additionally, a full shear connection is generally applied in actual composite bridges. The corresponding design guidance for the composite bridges with a full shear connection is given in design codes.

Therefore, an extremely large shear connection stiffness is applied to the proposed fiber beam element model to simulate complete interaction at the interface for the actual composite bridges in the following parametric analysis.

Before the parametric analysis, a mesh sensitivity test was performed. The results showed that the convergence sensitivities of the FE simulation results on the displacement and the stress are within 1% when 20 and 32 beam elements are used to mesh the composite beam, respectively. In order to ensure accuracy, a total of 50 elements and 51 nodes were used in the mesh.

4.1 Effective width based on the reinforcement stress

A reverse-loaded simply supported composite I-shape beam is used as a basic model to simulate the negative moment zone of continuous beams. The geometric dimensions and material properties of the basic model are shown in Table 1.

According to engineering experience, the longitudinal reinforcement ratio generally accounts for 1.5~2%, which is taken as 2% in the analysis. The concrete flange width is 500 mm, the effective span is 2500 mm and the width-span ratio is set to 0.2. For the calculation of the effective width of the negative moment zone, the design code does not consider the tensile strength of concrete, and such an assumption is applicable only under the ultimate states. Fig. 12 shows the transverse distribution of rebar stress at different cross-sections. The results show that there is an obvious shear lag effect at the mid-span section. The maximum stress in the rebar is reached at the intersection of the steel web and the concrete slab and decreases continuously from the center to the two sides. Therefore, it is of great significance to calculate the stress in the reinforcements above the steel girder by using a more accurate effective flange width. The following formula (Eq. (21)) is adopted in this paper to calculate the effective flange width of concrete slabs in the negative moment region.

$$\sigma_{\text{bar max}} = \frac{M y_{\text{bar}}}{I_{\text{tx}}} \tag{21}$$

Table 1 Parameters of the FE model

Structure		Span L (mm)	2500
Cross-section	Concrete slab	Slab width b_c (mm)	500
		Slab thickness t_c (mm)	50
	Reinforcement	Ratio	2%
	Steel girder	Flange width b_{st} (mm)	170
		Flange thickness t_{st} (mm)	15
		Web thickness t_w (mm)	9.5
		Web height h_s (mm)	470
Material	Concrete	Elastic modulus E_c (MPa)	3.35×10^4
		Grade	C50
	Steel	Elastic modulus E_s (MPa)	2.0×10^5
		Yield strength f_s (MPa)	345
	Reinforcement	Elastic modulus E_s (MPa)	2.0×10^5
		Yield strength f_{yr} (MPa)	350

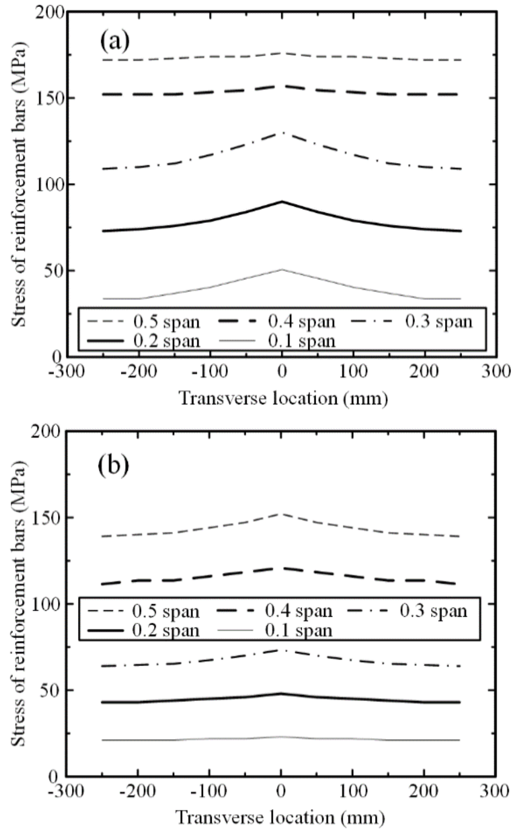

Fig. 12 Transverse distribution of rebar stress at different cross-sections: (a) uniformly distributed load; (b) concentrated load at mid-span

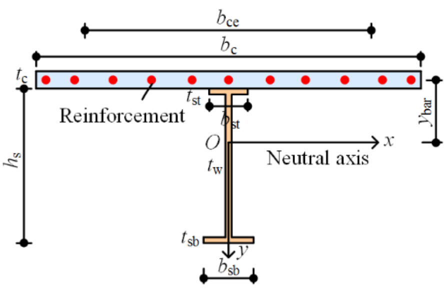

Fig. 13 Schematic diagram for effective flange width calculation

where $\sigma_{\text{bar max}}$ is the maximum stress in the reinforcements, which generally exists in the reinforcements adjoining the steel girder; M is the moment at the mid-span section; y_{bar} is the distance from the longitudinal steel bar to the neutral axis in the effective cross-section; and I_{tx} is the effective inertial moment of the composite beam, as shown in Fig. 13. The reinforcement layer is located in the center of the concrete slab, and the thickness of this layer is calculated according to the principle of area equivalence of the longitudinal reinforcing steel bar in the cross-section. The values of $\sigma_{\text{bar max}}$ and M can be obtained from the analytical results from the proposed model. The parameters y_{bar} and I_{tx} can be deduced as two expressions with respect to the

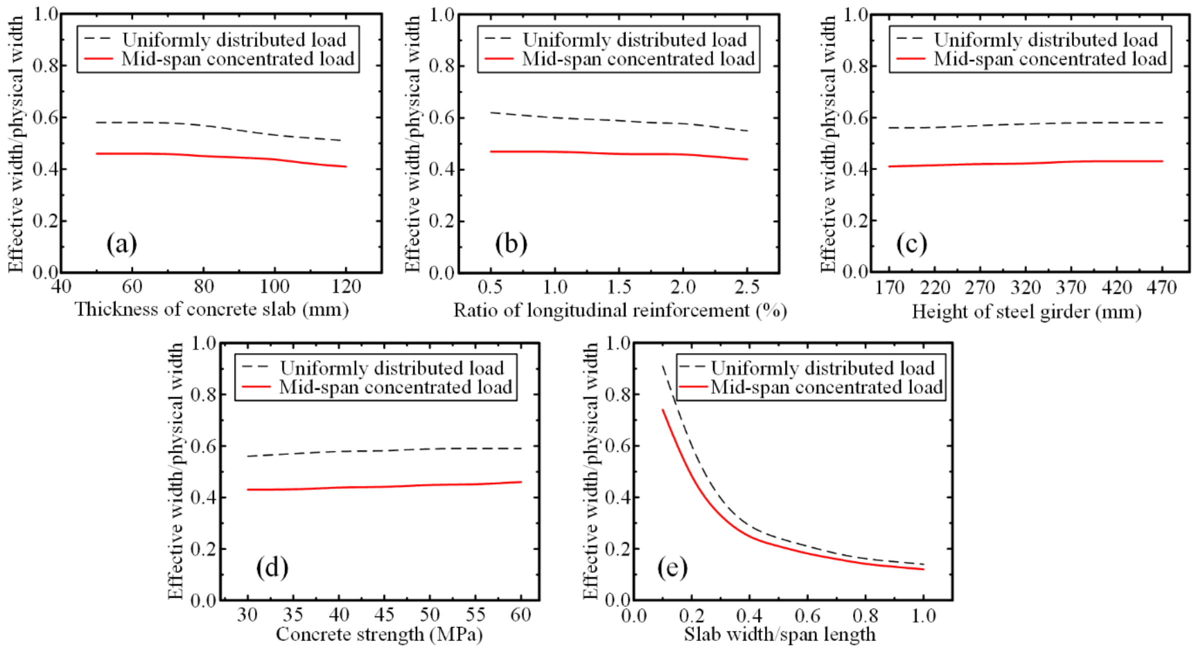

Fig. 14 Sensitivity analysis of the effective flange width coefficient: (a) thickness of concrete slab, (b) ratio of longitudinal reinforcement, (c) height of steel girder, (d) concrete strength grade and (e) slab width/span length

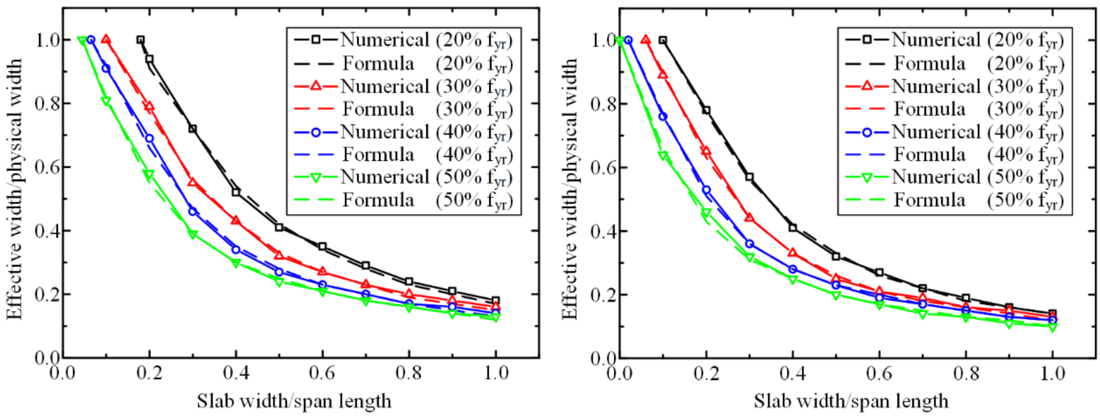

Fig. 15 Effective width comparisons of the proposed formula results and the numerical results: (a) uniformly distributed load and (b) concentrated load at mid-span

effective flange width b_{ce}, and the specified derivation can be found in the Appendix.

Substituting y_{bar}, I_{tx}, $\sigma_{bar\,max}$ and M into Eq. (21), a cubic equation of b_{ce} can be established, and the value of the effective flange width b_{ce} can be obtained with the solution of the equation. A dimensionless scalar named as effective width coefficient, which is herein defined as the ratio of effective width to physical width (b_{ce}/b_c), is adopted in the study.

4.2 Parametric analysis

According to the practice experiment, the reinforcement stress will not exceed 50% yield stress but may be less than 30% yield stress in the normal service stage. The effective flange width is larger with a smaller reinforcement stress than with a larger reinforcement stress. For security reasons, the authors choose the stages of 20~50% longitudinal reinforcement yield stress as the basis of determining effective width in the normal service stage.

The effects of the concrete slab thickness, longitudinal reinforcement ratio, steel girder height, concrete strength grade and width-span ratio on the effective width are fully analyzed and discussed. In every case, the effective width at the mid-span section was calculated at the stage when the longitudinal reinforcement stress reached 20%, 30%, 40% and 50% yield stress. Two loading patterns, including uniform loading and centralized loading at the mid-span, are considered. The interfacial slip effect is neglected during this analysis work because the slip in actual composite bridges is very small for composite beams. In this section, the detailed analysis process is written for the stage of 50% longitudinal reinforcement yield stress; the results in the other stages are similar. The effects of different parameters are discussed hereafter.

(1) Concrete slab thickness: In these cases, the concrete slab thickness varies from 50~120 mm, whereas the other parameters remain unchanged. With the variation in slab thickness, the location of the reinforcement layer varies accordingly to keep in the middle layer of the concrete slab. The analysis results are shown in Fig. 14(a).

(2) Longitudinal reinforcement ratio: In these cases, 10 different longitudinal reinforcement ratios varying from 0.5~2.5% are discussed, and the other parameters remain unchanged, as shown in Table 1. The variation in the effective width is shown in Fig. 14(b).

(3) Height of steel girder: Seven cases with different steel girder heights (from 170 mm to 470 mm) are considered to study the corresponding effects on effective width, as shown in Fig. 14(c).

(4) Concrete strength grade: The effects of the concrete strength grade on the effective width are discussed with the interval of 30~60 MPa (compressive strength of a 150 mm×150 mm×150 mm cube), as shown in Fig. 14(d).

(5) Width-span ratio: The computed span (2500 mm) is held constant, and the effects of the width-span ratio on the effective width are discussed. The analytical results are shown in Fig. 14 (e).

Based on the results of the parametric analysis, some regularity can be observed and concluded. The effective width coefficient decreases with increasing concrete slab thickness and longitudinal reinforcement ratio, but the effects are not significant. With increasing web height and concrete strength grade, the effective width coefficient increases slightly. The width-span ratio has a notable effect on the effective width, and the effective width coefficient decreases with increasing width-span ratio. Moreover, the loading pattern is the other important factor for the effective width. The effective width coefficient under uniform load is larger than that under concentrated load, whereas the trend is the same.

4.3 Simplified formula for effective width

According to the results of the parametric analysis, the width-span ratio and loading pattern are considered the main factors on the effective width. Therefore, the other parameters are not considered in this section due to their weak influence. The numerical results of the effective width coefficient at the stages of 20~50% longitudinal reinforcement yield stress are shown in Fig. 15. The effective width coefficient decreases with increasing reinforcement stress under both loading patterns. The reason for this behavior is that the cracking area of the concrete slab increases gradually with increasing reinforcement stress, leading to a decreasing effective width. In addition, the results show that the effective width coefficients are quite different under the four stress stages for the cases with a small width-span ratio. The maximum difference in the effective width coefficients is approximately 0.2 when the width-span ratio is 0.1. As the width-span ratio increases, the difference in the effect width coefficients decreases gradually, and the maximum difference in the effective width coefficients is 0.1 when the width-span ratio is 1.0. According to the physical significance, the effective width should be close to the actual concrete slab width when the width-span ratio approaches zero.

Based on the numerical analysis results from the proposed model, the effective flange width coefficients of the concrete slabs at different stages are calculated. Then, the simplified formulas for the effective width coefficients at different stages are proposed by fitting with the least-squares method. The formulas are proposed hereafter.

(1) Uniformly distributed load

Stage of 20% yield stress:
$$\frac{b_{\mathrm{ce}}}{b_{\mathrm{c}}} = 1 - e^{-0.186(b_{\mathrm{c}}/L)^{-1.589}} \tag{24a}$$

Stage of 30% yield stress:
$$\frac{b_{\mathrm{ce}}}{b_{\mathrm{c}}} = 1 - e^{-0.156(b_{\mathrm{c}}/L)^{-1.402}} \tag{24b}$$

Stage of 40% yield stress:
$$\frac{b_{\mathrm{ce}}}{b_{\mathrm{c}}} = 1 - e^{-0.138(b_{\mathrm{c}}/L)^{-1.276}} \tag{24c}$$

Stage of 50% yield stress:
$$\frac{b_{\mathrm{ce}}}{b_{\mathrm{c}}} = 1 - e^{-0.133(b_{\mathrm{c}}/L)^{-1.115}} \tag{24d}$$

(2) Concentrated load at mid-span

Stage of 20% yield stress:
$$\frac{b_{\mathrm{ce}}}{b_{\mathrm{c}}} = 1 - e^{-0.146(b_{\mathrm{c}}/L)^{-1.451}} \tag{25a}$$

Stage of 30% yield stress:
$$\frac{b_{\mathrm{ce}}}{b_{\mathrm{c}}} = 1 - e^{-0.130(b_{\mathrm{c}}/L)^{-1.256}} \tag{25b}$$

Stage of 40% yield stress:
$$\frac{b_{\mathrm{ce}}}{b_{\mathrm{c}}} = 1 - e^{-0.126(b_{\mathrm{c}}/L)^{-1.068}} \tag{25c}$$

Stage of 50% yield stress:
$$\frac{b_{\mathrm{ce}}}{b_{\mathrm{c}}} = 1 - e^{-0.116(b_{\mathrm{c}}/L)^{-0.972}} \tag{25d}$$

In the equations above, the range of the width-span ratio b_c/L is 0.1~1.0.

The fitting results under different load types and stress stages show a good correlation, wherein the coefficient of determination R^2 is close to 1. Therefore, these simplified formulas can be used to calculate the effective flange width.

4.4 Simplified design method

In the negative moment region of composite beams, the effective width of the concrete slabs is determined by the longitudinal reinforcement stress, while the effective width calculation is also needed to obtain the reinforcement stress. Therefore, a simplified iteration method for calculating the maximum longitudinal reinforcement stress based on the effective flange width is proposed. The maximum bending moment of the span in the normal service stage is obtained through the most unfavorable load cases of actual composite bridges. Then, the reasonable effective width and the longitudinal reinforcement stress can be obtained by using the cyclic iteration method. The calculation flowchart is shown in Fig. 16.

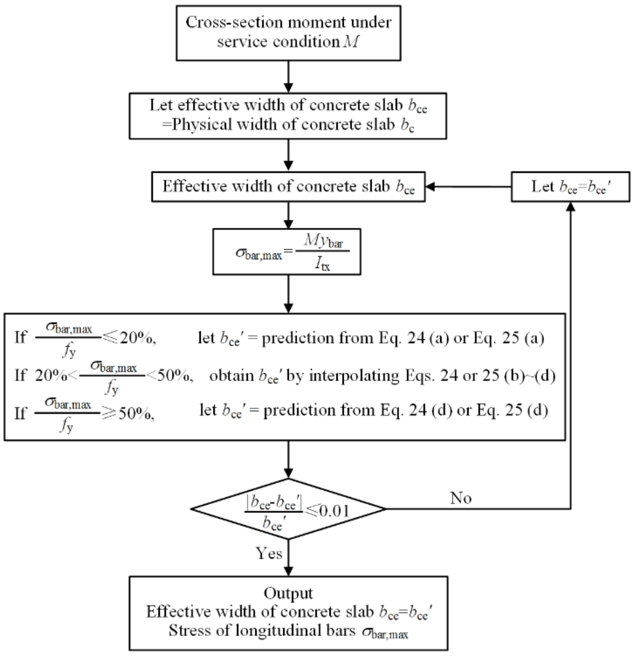

Fig. 16 Flowchart of the simplified reinforcement stress calculation method

Hereafter, some tips are mentioned for the reinforcement stress calculation process. For the cases in which the longitudinal reinforcement stress is less than 20% yield stress, the structure is basically in the elastic stage, and the effective width formula in Eq. (24) or Eq. (25(a)) can be used. Based on practical experience, the longitudinal reinforcement stress is generally not greater than 50% in the normal use stage. Thus, the formula in Eq. (24) or Eq. (25(d)) can be used for cases greater than 50%. For cases of 20~50%, the interpolation method can be used to calculate the effective flange width.

4.5 Comparisons of the crack width between the proposed formulas and the design code

In the Chinese design code, the concrete tensile strength is not considered in the design of the negative moment region, which causes an overestimation of longitudinal reinforcement stress. Therefore, the crack width in the concrete slab is also overestimated because the crack width specified in the design code is positively correlated with the reinforcement stress. Based on the simplified formulas and design method proposed in this paper, the crack width in the concrete is calculated, and the results are compared with those from the Chinese design code method (JTG 3362-2018).

The structural parameters of the analysis case are shown in Table 1, for which the width-span ratio is 0.2 and a 405 kN·m negative moment occurs at the mid-span. Comparisons of the longitudinal reinforcement stress and concrete crack width in the simplified formulas and the design code are shown in Table 2.

Table 2 Comparison of the results from the simplified formulas and the design code

		Longitudinal reinforcement stress (MPa)	Concrete crack width (mm)
Uniformly distributed load	Simplified method	154.55	0.12
	Design code	253.13	0.19
Concentrated load at mid-span	Simplified method	181.62	0.14
	Design code	253.13	0.19

The results clearly show that the stress calculated by the simplified method in this paper is approximately half of the reinforcement yield stress, which indicates that the composite beam is still in the normal service stage. In contrast, the stress obtained by the design code, which neglects the contribution of concrete, reaches 70% of the yield stress. With respect to the concrete crack width, the results calculated by the design code method are close to 0.2 mm when neglecting the contribution of concrete. With the same loading states, the results of the concrete crack width obtained by the simplified method in this paper are only 0.12 mm and 0.14 mm. Therefore, the concrete crack width obtained by the design code is at most 60% larger than that obtained by the proposed method. The crack width calculated by the design code method is close to the maximum crack width limit specified in code (for a type-I environment), which is obviously not reasonable.

5. Conclusions

In this paper, the effective flange width of steel-concrete composite beams in the normal service stage is systematically studied, and the specific work is concluded as follows:

- A fiber beam element model for composite beams considering the shear lag effect and interfacial slip effect is proposed, and the accuracy and applicability of the model are fully verified by comparisons with experiments of composite beams under positive and negative moment loading states.
- The calculation method of effective width in the negative moment region is proposed on the basis of longitudinal reinforcement stress. Based on the proposed model, the effects of different parameters, including the width-span ratio, concrete slab thickness, longitudinal reinforcement ratio, steel girder web height and concrete strength grade, on the effective flange width in the negative moment region in the normal service stage are analyzed and discussed. A simplified formula for calculating the effective width is proposed for the negative moment region at the stages of 20~50% reinforcement yield stress.
- Based on the simplified effective width formula, a simplified calculation method is proposed for the

reinforcement stress in the negative moment region of composite beams in the normal service stage. The corresponding reinforcement stress and concrete crack width are obtained and compared with those calculated by the formula recommended in the code. This comparison shows that the design code method completely neglects the stiffness contribution of the concrete, which makes the results calculated by the design code significantly larger than those calculated by the proposed method. The concrete crack width obtained by the proposed simplified analysis method is approximately 61% and 73% of those obtained by the design code for the uniformly distributed load case and the concentrated load case at mid-span, respectively.

Acknowledgments

The authors gratefully acknowledge the financial support provided by the Fundamental Research Funds for the Central Universities (2018JBZ106), the National Natural Science Foundation of China (51608031) and the Technical and Development Project of Shuohuang Railway Development Co., Ltd. (SHTL-19-14).

References

Amadio, C. and Fragiacomo, M. (2002), “Effective width evaluation for steel-concrete composite beams”, *J. Constr. Steel. Res.*, **58**, 373–388. 10.1016/S0143-974X(01)00058-X.

Amadio, C., Fedrigo, C., Fragiacomo, M. and Macorini, L. (2004), “Experimental evaluation of effective width in steel-concrete composite beams”, *J. Constr. Steel. Res.*, **60**, 199-220. 10.1016/j.jcsr.2003.08.007.

CEB-FIP (2010), Model Code 2010, First complete draft, vol. 1, International Federation for Structural Concrete (fib), Lausanne, Switzerland.

Chen, S.S., Aref, A.J., Chiewanichakorn, M. and Ahn, I.S. (2007), “Proposed effective width criteria for composite bridge girders”, *J. Bridge Eng.*, **12**(3), 325-338. 10.1061/(asce)1084-0702(2007)12:3(325).

Chiewanichakorn, M., Aref, A.J., Chen, S.S. and Ahn, I. (2004), “Effective flange width definition for steel-concrete composite bridge girder”, *J. Struct. Eng.*, **130**(12), 2016-2031. 10.1061/(ASCE)07339445(2004) 130:12(2016).

Dezi, L., Gara, F. and Leoni, G. (2003), “Shear-lag effect in twin-girder composite decks”, *Steel Compos. Struct.*, **3**(2), 111-122. https://doi.org/10.12989/scs.2003.3.2.111.

Dezi, L., Gara, F. and Leoni, G. (2006), “Effective slab width in prestressed twin-girder composite decks”, *J. Struct. Eng.*, **132**(9), 1358-1370. 10.1061/(ASCE)07339 445(2006)132:9(1358).

Eurocode (2004), Design of Composite Steel and Concrete Structures. Part 2: General Rules and Rules for Bridges, European Committee for Standardization; Brussels, Belgium.

Gandelli, E., Penati, M., Quaglini, V., Lomiento, G., Miglio E. and Benzoni, G.M. (2019), “A novel OpenSees element for single curved surface sliding isolators”, *Soil Dyn. Earthq. Eng.*, **119**, 433-453. 10.1016/j.soildyn. 2018.01.044.

Gara, F., Leoni, G. and Dezi, L. (2009), “A beam finite element including shear lag effect for the time-dependent analysis of steel-concrete composite decks”, *Eng. Struct.*, **31**(8), 1888-1902. 10.1016/j.engstruct.2009.03.017.

Gara, F., G Ranzi, G. and Leoni, G. (2011), “Partial interaction analysis with shear-lag effects of composite bridges: a finite element implementation for design applications”, *Adv. Steel Constr.*, **7**(1), 1-16. 10.18057/ijasc.2011.7.1.1.

Hognestad, E., Hanson, N.W. and McHenry, D. (1955), “Concrete stress distribution in ultimate strength design”, *ACI J. Proceedings*, **52**(12), 455-480.

JTG 3362-2018 (2018), Code for Design of Highway Reinforced Concrete and Prestressed Concrete Bridges and Culverts. Ministry of Transport of PRC, Beijing, China. (in Chinese)

Lezgy-Nazargah, M, and Kafi, L. (2015), “Analysis of composite steel-concrete beams using a refined high-order beam theory”, *Steel Compos. Struct.*, **18**(6), 1353-1368. https://doi.org/10.12989/scs.2015.18.6.1353.

Lezgy-Nazargah, M., Vidal, P. and Polit, O. (2019), “A sinus shear deformation model for static analysis of composite steel-concrete beams and twin-girder decks including shear lag and interfacial slip effects”, *Thin-Wall. Struct.*, **134**, 61-70. 10.1016/j.tws.2018.10.001.

Li F.X. (2011), “Spatial Structural behavior and time-dependent analysis of composite cable stayed bridge”, Ph.D. Dissertation, Tsinghua University, Beijing. (in Chinese)

Lin, Z. and Zhao, J. (2012), “Modeling inelastic shear lag in steel box beams”, *Eng. Struct.* **41**, 90-97. 10.1016/j.engs truct.2012.03.018.

Lin, W. and Yoda, T. (2013), “Experimental and numerical study on mechanical behavior of composite girders under hogging moment”, *Adv. Steel Constr.*, **9**(4), 309-333. 10.18057/IJASC.2013.9.4.4.

Luo, D., Zhang, Z. and Li B. (2019), “Shear lag effect in steel-concrete composite beam in hogging moment”, *Steel Compos. Struct.*, **31**(1), 27-41. https://doi.org/10.12989/scs.201 9.31.1.027.

Ma, Y., Ni, Y.S., Xu, D. and Li, J.K. (2017), “Space grid analysis method in modelling shear lag of cable-stayed bridge with corrugated steel webs”, *Steel Compos. Struct.*, **24**(5), 549-559. https://doi.org/10.12989/scs.2017.24.5.549.

Nie, J.G., Tian, C.Y. and Cai, C.S. (2008), “Effective width of steel-concrete composite beam at ultimate strength state”, *Eng. Struct.*, **30**, 1396-1407. 10.1016/j.engstruct.200 7.07.027.

Ollgaard, J.G., Slutter, R.G. and Fisher, J.W. (1971), “Shear strength of stud connectors in lightweight and normal weight concrete”, *AISC Eng. J.*, **8**(2), 495-506.

Ranzi, G. and Bradford, M.A. (2006), “Analytical solutions for the time-dependent behaviour of composite beams with partial interaction”, *Int. J. Solid. Struct.*, **43**(13), 3770-3793. 10.1016/j.ijsolstr.200 5.03.032.

Ranzi, G. and Bradford, M.A. (2009), “Analysis of composite beams with partial interaction using the direct stiffness approach accounting for time effects”, *Int. J. Numer. Method. Eng.*, **78**(5), 564-586. 10.1002/nme.2500.

Vojnić-Purčar, M., Prokić, A. and Bešević, M. (2019), “A numerical model for laminated composite thin-walled members with openings considering shear lag effect”, *Eng. Struct.*, **185**, 392-399. 10.1016/j.engstruct.201 9.01.142.

Wendner, R., Vorel, J., Smith, J., Hoover, C.G., Bažant, Z.P. and Cusatis, G. (2015), “Characterization of concrete failure behavior: a comprehensive experimental database for the calibration and validation of concrete models”, *Mater. Struct.*, **48**(11), 3603-3626. 10.1617/s11527-014-0426-0.

Yoon, K., Lee, P.S. and Kim, D.N. (2017), “An efficient warping model for elastoplastic torsional analysis of composite beams”, *Compos. Struct.*, **178**, 37-49. 10.1016/j.compstruct.2017.07.041.

Zhu, L., Nie, J.G., Li, F.X. and Ji, W.Y. (2015), “Simplified analysis method accounting for shear-lag effect of steel-concrete composite decks", *J. Constr. Steel. Res.*, **115**(7), 62-80. 10.1016/j.jcsr.2015.08.020.

Zhu, L. and Su, R.K.L. (2017), "Analytical solutions for composite beams with slip, shear-lag and time-dependent effects", *Eng. Struct.*, **152**, 559-578. 10.1016/j.engstruct.2017.08.071.

CC

Appendix

The thickness of reinforcement layer $t_r = A_r/b_c$, in which A_r is the total area of reinforcements.

Equivalent sectional area moment

$$\begin{aligned} S_t &= \left(b_{ce}t_c/n + b_{ce}t_r\right)\left(t_c/2 + h_w\right) + b_{st}t_{st}\left(h_s - t_{st}/2\right) \\ &\quad + b_{sb}t_{sb}t_{sb}/2 + t_w\left(h_s - t_{st} - t_{sb}\right)\left(h_s/2 + t_{sb}/2 - t_{st}/2\right) \end{aligned} \tag{26}$$

Equivalent sectional area:

$$A_t = b_{ce}t_c/n + b_{ce}t_r + b_{st}t_{st} + b_{sb}t_{sb} + t_w\left(h_s - t_{st} - t_{sb}\right) \tag{27}$$

Distance between the lower flange bottom edge of the steel girder and the neutral axis of the equivalent cross-section

$$y_t = S_t / A_t \tag{28}$$

Distance between the rebar layer and the neutral axis in the equivalent cross-section

$$y_{bar} = t_c/2 + h_s - y_t \tag{29}$$

Inertia moment of equivalent cross-section

$$\begin{aligned} I_{tx} &= b_{ce}t_c^3/\left(12n\right) + b_{ce}t_c y_{bar}^2/n + b_{ce}t_r^3/12 \\ &\quad + b_{ce}t_r y_{bar}^2 + b_{st}t_{st}^3/12 + b_{st}t_{st}\left(h_s - t_{st}/2 - y_t\right)^2 \\ &\quad + b_{sb}t_{sb}^3/12 + b_{sb}t_{sb}\left(t_{sb}/2 - y_t\right)^2 + t_w\left(h_s - t_{st} - t_{sb}\right)^3/12 \\ &\quad + t_w\left(h_s - t_{st} - t_{sb}\right)\left(h_s/2 - t_{st}/2 + t_{sb}/2 - y_t\right)^2 \end{aligned} \tag{30}$$

Maximum longitudinal reinforcement stress

$$\sigma_{bar\,max} = \frac{M y_{bar}}{I_{tx}} \tag{31}$$